

Article

# Dynamic Response of Paper-Based Bi-Material Cantilever Actuator

Ashutosh Kumar \* , Jun Hatayama, Nassim Rahmani, Constantine Anagnostopoulos and Mohammad Faghri \*

Microfluidics Laboratory, Department of Mechanical, Industrial and Systems Engineering, University of Rhode Island, 2 East Alumni Avenue, Kingston, RI 02881, USA; jun.hatayama@uri.edu (J.H.); nara7@uri.edu (N.R.); anagnostopoulos@uri.edu (C.A.)

\* Correspondence: ashutosh@uri.edu (A.K.); faghri@uri.edu (M.F.)

**Abstract:** This work presents a dynamic modeling approach for analyzing the behavior of a bi-material cantilever actuator structure, consisting of a strip of filter paper bonded to a strip of tape. The actuator's response is induced by a mismatch strain generated upon wetting, leading to the bending of the cantilever. The study delves into a comprehensive exploration of the dynamic deflection characteristics of the bilayer structure. It untangles the intricate connections among the saturation, modulus, hygro-expansion strain, and deflection, while uniquely addressing the challenges stemming from fluid–structure coupling. To solve the coupled fluid–solid differential equations, a combined numerical method is employed. This involves the application of the Highly Simplified Marker and Cell (HSMAC) technique for fluid flow analysis and the Finite Difference Method (FDM) for response deflection computation. In terms of the capillary flow model, the Computational Fluid Dynamics (CFD) simulations closely align with the classical Washburn relationship, depicting the wetted front's evolution over time. Furthermore, the numerical findings demonstrate that heightened saturation levels trigger an increase in hygro-expansion strain, consequently leading to a rapid rise in response deflection until a static equilibrium is achieved. This phenomenon underscores the pivotal interplay among saturation, hygro-expansion strain, and deflection within the system. Additionally, the actuator's response sensitivity to material characteristics is highlighted. As the mismatch strain evolving from paper hygro-expansion diminishes, a corresponding reduction in the axial strain causes a decrease in response deflection. The dynamic parameter demonstrates that the deflection response of the bilayer actuator diminishes as dynamic pressure decreases, reaching a minimal level beyond which further changes are negligible. This intricate correlation underscores the device's responsiveness to specific material traits, offering prospects for precise behavior tuning. The dependence of paper modulus on saturation levels is revealed to significantly influence bilayer actuator deflection. With higher saturation content, the modulus decreases, resulting in amplified deflection. Finally, strong concordance is observed among the present fluidically coupled model, the static model, and empirical data—a testament to the accuracy of the numerical formulation and results presented in this study.



**Citation:** Kumar, A.; Hatayama, J.; Rahmani, N.; Anagnostopoulos, C.; Faghri, M. Dynamic Response of Paper-Based Bi-Material Cantilever Actuator. *Micro* **2023**, *3*, 785–810. <https://doi.org/10.3390/micro3040056>

Academic Editor: Nicola Pio Belfiore

Received: 2 September 2023

Revised: 9 October 2023

Accepted: 21 October 2023

Published: 24 October 2023

**Keywords:** paper-based sensors; bilayer actuators; microfluidic assay; biosensing; hygro-expansion; modulus of paper; dynamic curvature; couple fluid–structure model



**Copyright:** © 2023 by the authors. Licensee MDPI, Basel, Switzerland. This article is an open access article distributed under the terms and conditions of the Creative Commons Attribution (CC BY) license (<https://creativecommons.org/licenses/by/4.0/>).

## 1. Introduction

Bilayer cantilevers, particularly those consisting of two distinct materials, have come to the forefront of scientific research due to their unique bending behaviors when exposed to varying stimuli [1,2]. Historically, Christophersen et al. delved into the modeling of PPy bilayer micro-actuators, bringing valuable insights into the realm of microfluidic devices [3]. This research pathway found resonance with our contemporary work, in which we presented an extensive study on a paper-based bi-material cantilever (B-MaC) valve and innovated a lab-on-paper microfluidics platform using bi-material cantilever actuators [4,5].

Environmental factors, such as temperature and humidity, can significantly influence the curvature of these bilayer cantilevers [6,7]. Douezan et al. laid the foundational knowledge in understanding this interaction by studying the hygro-mechanical bending response of paper when it encounters water [8]. These studies were further augmented by Perez-Cruz et al., who unveiled the intriguing curling instability introduced by swelling [9]. Reyssat and Mahadevan's exploration into the curling behavior of wet paper further enriched our understanding of paper-based cantilevers, offering pivotal insights for microfluidic paper-based assays [10]. Applications in biosensing have found significant traction in the utilization of bilayer cantilevers. Groundbreaking research by Wang et al. highlighted the scope of microcantilever sensors in biochemical detection [11]. The versatility and immense potential of cantilever-based technologies have been underlined by studies spanning across lab-on-a-chip integrations to aptamers targeting membrane proteins for diagnostics [12–14]. Significantly, the work of Kaigala et al. accentuated the utility of microfluidics in enabling localized chemistry on biological interfaces, potentially transforming diagnostic paradigms [15].

Recent advancements in this domain have emphasized the need for rigorous modeling. This modeling aids in predicting the behavior of these bilayer cantilevers under multifaceted stimuli [16]. For instance, Rasid et al. conducted in-depth dynamic modeling of micro-lens actuators, emphasizing the need for intricate modeling in designing cantilever-based devices [17]. Yang et al.'s studies on the modeling and nonlinear dynamics of various cantilever actuators offer perspectives on device behavior under different scenarios, paving the way for design optimization [18]. Lee et al. emphasized the critical role of material properties in cantilever-based devices by employing a quasi-static theoretical framework and corroborating their model through quantitative experimental data [19].

In the realm of paper-based cantilevers, understanding the intricacies of fluid flow is of paramount importance, especially when aiming for the precise control and prediction of the cantilever's response. The Navier–Stokes equations, which govern the motion of viscous fluid substances, have been invaluable in depicting the nuances of fluid mechanics within such structures. The computational modeling landscape for fluid dynamics has notably been enriched by advancements in Computational Fluid Dynamics (CFD). Albadawi et al. took strides in examining the influence of surface tension within the Volume of Fluid (VOF) models and their hybrid applications alongside the Level Set methods, laying a foundation for better understanding bubble dynamics within fluid structures [20]. The continuum method by Brackbill et al. also delved deep into modeling surface tension, a critical parameter for the behavior of fluids within the microstructures of paper-based cantilevers [21]. Furthermore, the relevance of flows, as expounded by Kajishima, plays a significant role in comprehending the often-complex fluid behaviors in these bi-material devices, underscoring the need for holistic modeling approaches [22]. Together, these advancements in fluid modeling, epitomized by Navier–Stokes formulations and CFD methodologies, provide a comprehensive lens to unravel the dynamic behaviors of paper-based cantilevers when interacting with fluids.

Despite the plethora of research available, with studies ranging from organ-on-chip technologies to diverse applications beyond biology [23], the central theme remains, understanding the dynamic interactions between fluid and structure in these bi-material cantilevers, particularly paper-based ones. This understanding, centered around the dynamic coupled fluid–structure model for response deflection, is imperative to harness the full potential of bi-material cantilevers (B-MaCs) in microfluidic paper-based assays for biosensing and other applications. This manuscript seeks to address this niche, focusing specifically on the dynamic coupling of fluid and structural models in understanding deflection responses.

Our previous studies [1,2,4,5,24] were geared towards the creation of a quasi-static model to scrutinize both the deflection response and fluidic behavior of B-MaCs under static conditions, accounting for parametric variations induced by saturation. As can be seen from the referenced literature [6–10,19], very few studies have focused on dynamic modeling, primarily concentrating instead on static formulations for bilayer cantilevers with constant

parameters. Notable investigations, such as those detailed in [25–27], delve into various facets of dynamic responses, ranging from nonlinear bending behaviors in piezoelectric actuators to hydrodynamic interactions in microcantilevers. These comparative studies accentuate the importance of a holistic approach in understanding the dynamic behaviors of bi-material cantilevers, spotlighting the intricate interplay between material properties, external stimuli, and the resulting responses.

The incentive of this work is to further develop the dynamic model for response deflection of a coupled fluid and structure bilayer system. This dynamic approach has been realized through an intricate coupling of fluid mechanics, governed by the Navier–Stokes equations, with the mechanical properties of bilayer cantilevers. This study significantly advances the field by incorporating hygro-expansive behavior and variable material properties into a comprehensive model. This enables far more accurate predictions and provides deeper insights into the complex interactions within the system under fluid loading. Additionally, our adopted methodology shows great versatility, accommodating various material types and levels of saturation. This research offers a notable advantage by integrating dynamic methodologies with variable properties, providing a more comprehensive perspective than traditional approaches. This enhances its relevance for a multitude of applications, from biosensors to material testing procedures. The approach surpasses traditional methods by facilitating numerical solutions for intricate systems where closed-form solutions are not feasible. It marks a pivotal advancement, integrating sophisticated numerical methods like the Highly Simplified Marker and Cell (HSMAC) approach and the Finite Difference Method (FDM) to solve complex fluid–structure interaction problems with broader applicability.

## 2. Methods

To effectively understand the behavior of bi-material cantilever (B-MaC) subjected to fluid flow, there is an inherent need to couple fluid–structure models. This not only provides a comprehensive view of the mechanisms but also allows for the creation of nuanced and precise predictive tools. This section outlines our approach towards creating such a coupled model.

### 2.1. Response Deflection

In our investigation of flow dynamics within the B-MaC, several critical assumptions rooted in the theory are applied. Initially, B-MaC structures are presumed straight, with subsequent curvatures introduced purely due to fluid loading. These structures maintain that cross-sections remain planar even after bending. Emphasizing the material properties, B-MaC adheres to a linear elastic behavior, implying compliance with Hooke’s law, while also being isotropic and homogenous in nature. This ensures consistent stress–strain dynamics throughout the structure, regardless of direction or location. It is important to note that the bonding in our bilayer system, primarily contributed by the adhesive layer of the Scotch tape, ensures cohesive interactions between the layers. This adhesive layer’s nuances, although not separately analyzed, are inherently incorporated within the combined behavior of our bilayer structure. While the B-MaC may undergo moderate deflections from fluid interactions, rotations are assumed minimal. Moreover, any shear deformation due to these interactions is considered negligible, focusing our attention primarily on bending deformations. Lastly, if any prestress is imposed on the B-MaC, it is uniformly distributed, ensuring each point within a cross-section experiences identical stress magnitudes inducing curvatures. Recognizing and considering these assumptions is paramount as we navigate our analytical framework and interpret subsequent results.

For slender beams experiencing moderate deflections, the dynamic beam differential equation provides a robust model to characterize structural behavior. The equation considering the beam under the effects of prestress upon dynamic loading, given below,

inherently considers the linear variation of strain across the cross-section and offers an accurate representation for moderate deflections [28].

$$\frac{\partial^4 w}{\partial x^4} - \zeta \frac{\partial^2 w}{\partial x^2} + \eta \frac{\partial^2 w}{\partial t^2} = q(x, t) \tag{1}$$

The presented equation delineates the dynamic behavior of the B-MaC under various influences. Here,  $w(x, t)$  signifies the dynamic deflection of the B-MaC, indicating how the actuator responds over time,  $t$ , and along its length,  $x$ . The above equation is written in the non-dimensional form of Equation (A4), as found in Appendix A, utilizing the parameter  $x$  represented as  $\frac{x}{L}$ , where  $L$  stands for the total length of the bilayer cantilever. This formulation allows for a universal representation, independent of specific system dimensions. The axial loading parameter,  $\zeta$ , quantifies the influence of the axial load on the system, determining how it might cause or influence deflections, and  $\eta$  provides a measure of the mass per unit length, capturing the inherent inertia of the B-MaC element. Lastly,  $q(x, t)$  represents the fluidic loading at any given time and position, factoring in fluid mass as an external force acting transverse to the B-MaC’s length. In Table 1, we present a comprehensive breakdown of the non-dimensional parameters utilized in our governing equation. Each of these parameters is pivotal in characterizing the interplay of forces and responses, shedding light on the B-MaC’s dynamic behaviors under diverse conditions.

**Table 1.** Parameters for modeling the response deflection of B-MaC.

Parameters	Expression	Description
$\zeta$	$\left(\frac{r_A \epsilon_o}{r_F}\right) L^2$	Hygro-expansion loading
$\eta$	$\left(\frac{m}{r_F}\right) L^4$	Mass element
$q$	$\left(\frac{\rho_f g A_p}{r_F}\right) L^4$	Fluidic loading

In a bilayer cantilever system with perfectly bonded conditions, the mechanical properties of both layers can be combined to analyze the overall behavior. The flexural rigidity  $r_F$ , axial rigidity  $r_A$ , and mass density  $m$ , take into account the contribution of both layers [29,30]. When transitioning from a monolayer to a bilayer system, certain modifications are imperative. For a bilayer setup, in a perfectly bonded condition  $r_F$ ,  $r_A$ , and  $m$ , are given by  $\sum E_i I_i$ ,  $\sum E_i A_i$  and  $\sum \rho_i A_i$  respectively, for  $i$ th layer. Given that our B-MaC has a rectangular cross-section as shown in Figure 1, its area can be represented as  $A_i = b \times h_i$ , where  $b$  and  $h$  are respective width and heights. Consequently, for such a rectangular cross-section, the corresponding moment of inertia, can be calculated using the formula  $I_i = \frac{bh_i^3}{12}$  for  $i$ th layer. These modifications highlight the distinct behaviors of monolayer versus bilayer systems and underscore the significance of each parameter in our model. Additionally,  $\epsilon_o$  stands for the effective strain due to bending and hygro-expansion inherent to the bilayer system obtained via misfit strain [24], and  $\rho_f$  designates the density of the loaded fluid.

### 2.2. Fluid Flow

Fluid dynamics in the B-MaC system are profoundly governed by the Navier–Stokes equations, shedding light on the fluid’s momentum and continuity. These equations, while intricate, are pivotal for understanding the nuanced flow patterns and how they interact with B-MaC’s structural elements. A significant aspect of fluid dynamics in this system is the fluid imbibition in paper-like materials, primarily driven by capillary action, often referred to as pore-level transport at the microscale. In our pursuit to deeply understand fluid imbibition in B-MaC, we prioritize modeling fluid flow in the filter paper layer, approaching it as a porous entity influenced by capillary dynamics. Our research draws heavily on the Capillary Model, harmonizing with the Lucas–Washburn relationship, for a

more coherent representation of fluid movement in the filter paper. Building on our prior studies and experimental findings [1,4,24], this manuscript presents a refined modeling approach for fluid flow. Specifically, we delve into the Lucas–Washburn flow within the paper, adopting the reduced One-Dimensional Navier–Stokes equation. This method particularly emphasizes flow capillarity, factoring in the influential roles of surface tension and drag forces by the set of equations given below.

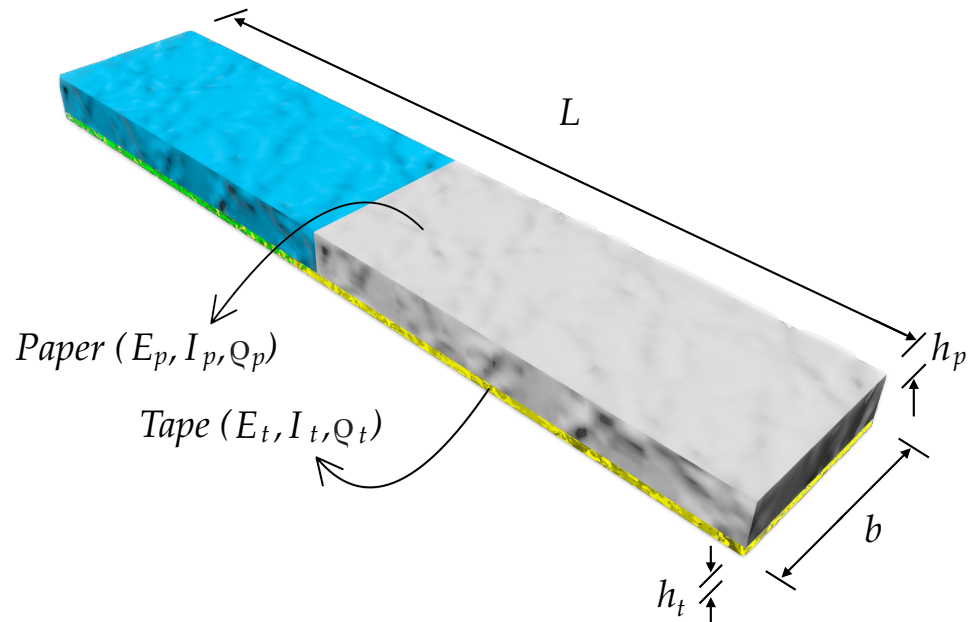


**Figure 1.** Bi-material cantilever (B-MaC) actuator utilized for modeling, fabricated via layer of Whatman Grade 41 filter paper and Scotch tape.

The 1-D N-S equation for VOF is the momentum conservation equation [20] as follows:

$$\frac{\partial u}{\partial t} + u \frac{\partial u}{\partial x} = -\frac{1}{\rho} \frac{\partial P}{\partial x} + \nu \frac{\partial^2 u}{\partial x^2} + \left( \frac{\sigma}{\rho r} \right) \frac{\partial a}{\partial x} - \left( \frac{v}{k} \right) u \tag{2}$$

Continuity Equation

$$\frac{\partial u}{\partial x} = 0 \tag{3}$$

Properties

$$\rho = (a)\rho_f + (1 - a) \rho_a \tag{4}$$

$$\nu = (a)\nu_f + (1 - a) \nu_a \tag{5}$$

The One-Dimensional N-S equation embodies the conservation of momentum within the fluid, factoring in the influences of advection, pressure gradients, viscous forces, surface tension, and drag forces. In the context of flows far from solid boundaries, drag forces are typically dominating, and the velocity gradients are not at their highest. In these regions, referred to as potential flow regions, viscous effects are negligible compared to the drag forces, and the term representing viscous force per unit mass  $\nu \frac{\partial^2 u}{\partial x^2}$ , can be ignored. This modification emphasizes that the drag forces are the primary concern. By utilizing this in conjunction with the continuity equation for incompressible flow  $\frac{\partial u}{\partial x} = 0$ , we can model one-dimensional fluid flow according to the VOF model for capillary flow. Please see

Figure 2 for details. This approach mirrors the Lucas–Washburn flow model, leading to the modification of Equation (2) for the wet region ( $a = 1$ ) as follows:

$$\frac{\partial u}{\partial t} = -\frac{1}{\rho_f} \frac{\partial P}{\partial x} + \left( \frac{\sigma}{\rho_f r} \right) \frac{\partial a}{\partial x} - u \left( \frac{v_f}{k} \right) \tag{6}$$

where  $\left[ \left( \frac{\sigma}{\rho_f r} \right) \frac{\partial a}{\partial x} \right]$  is due to the surface tension defined by the Continuum Surface Force (CSF) model [21]. The corrected Continuous Surface Force (C-CSF) methodology provides an interpretation of surface tension [31]. Notably, within the scope of our research, the term  $\sigma \cos \theta$  becomes simply  $\sigma$  for filter paper. This is because  $\theta$  representing the contact angle is small, leading to  $\cos \theta \sim 1$ . This characteristic highlights the pronounced hydrophilic nature of the filter paper in contact with water. The term  $\left[ u \left( \frac{v_f}{k} \right) \right]$  is the drag term as per Darcy’s Law [32],  $u$  is the velocity of fluid flow,  $\frac{\partial P}{\partial x}$  is the pressure gradient,  $\sigma$  corresponds to the surface tension of fluid,  $\rho_f$  is the density of fluid,  $r$  is the radius of the curvature of fluid interface in micro-capillary,  $\rho_a$  and  $v_a$  are the density and kinematic viscosity of air, respectively,  $\rho_f$  and  $v_f$  are the density and kinematic viscosity of water, respectively,  $k$  is the permeability paper, and  $a$  is the saturation level. The above Equation (6) will be subsequently solved numerically to obtain the solution for fluid flow with parameters  $C = \frac{\sigma}{r}$  and  $D = \frac{1}{k}$ .

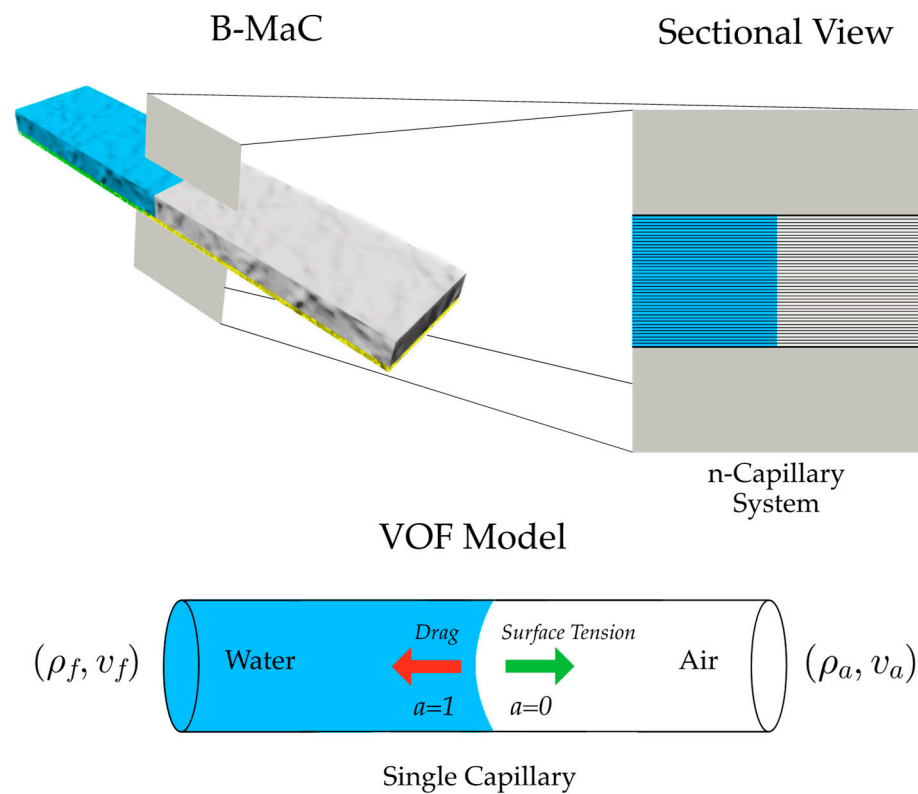


Figure 2. B-MaC sectional view—VOF model.

### 2.3. Coupled Fluid–Structure Model

Fluid flow in a bilayer structure is a complex phenomenon, particularly in the context of a composite beam made up of disparate materials. The coupled model developed in this study considers the fluid flow as a moving load, influencing both the internal forces through hygro-expansion and the external forces via transverse loading on the bilayer beam. To facilitate a tractable solution to this inherently dynamic problem, a new coordinate system is adapted for effectively rendering the dynamic problem into a static one. While various parameters of the beam altered due to fluidic loading are considered constant in the

dynamic phase, more significant variables such as modulus and strain become dependent on the saturation level. These are incorporated as key variables in the coupled model, allowing for a nuanced understanding of the interactions within the system.

The new coordinate system is adapted such that  $(x^1 = x - ut)$  and  $(w^1 = w)$  where  $x^1$  and  $w^1$  represent the new location of the load, and  $u$  is the velocity of fluid flow obtained from the N-S equation. This transformation modifies Equation (1), leading to the revised expression, given as follows:

$$\frac{d^4 w^1}{dx^{14}} + (\eta u^2 - \zeta) \frac{d^2 w^1}{dx^{12}} = q_0 \delta(x^1) \tag{7}$$

where the RHS of Equation (7) signifies the static load ( $q_0 = q$ ) acting at  $x^1$ .

The adapted coordinate system simplifies the problem by converting the moving load’s dynamics into a static frame, making it solvable. Without this transformation, the equation does not have a closed-form solution and requires further simplification. Consequently, we will adopt numerical methods to approach the given problem, which allows us to model the complex interactions between the fluid flow and the bilayer beam. Detailed explanations and the numerical solution strategy will be presented in the subsequent sections.

By describing the entire problem inclusive of the boundary conditions for the cantilever beam, at fixed end:  $w(0) = 0$  and  $w'(0) = 0$ , at free end:  $w''(1) = 0$  and  $w'''(1) = 0$ , and introducing  $\lambda_n^2 = (\eta u^2 - \zeta)$ , the following formulation is obtained for a given  $n$ -coordinate system:

$$w^{n''''} + \lambda_n^2 w^{n''} = q_0 \delta(x^n) \tag{8}$$

There are numerous tools and methodologies available for solving complex problems, such as the Fluid–Structure Interaction (FSI) technique. However, employing the FSI technique for our specific problem would be excessively intricate due to its inherent complexity and computational demands, particularly when modeling the intricate interaction between hydrophilic and hydrophobic materials in a bilayer structure. Instead, we have opted to utilize a combination of Computational Fluid Dynamics (CFD) coupled with the Finite Difference Method (FDM). This approach aligns more suitably with our problem’s characteristics and constraints, offering a more efficient and accurate solution. The details of this chosen method and the presentation of results will be articulated in the subsequent sections.

#### 2.4. Dependency of Bilayer Cantilever Material Properties on Fluid Loading

The behavior of a bilayer cantilever, especially when comprised of hygroscopic materials like paper, is notably influenced by its surrounding environment. When such a cantilever is exposed to fluid loading, it experiences variations in its saturation level ( $a$ ), leading to alterations in its inherent material properties. This phenomenon is even more pronounced in materials like paper, which has a pronounced affinity for moisture, and the adhesive nature of tape, which might act as a barrier or a conduit for moisture ingress, depending on the B-MaC fabrication. Understanding this dependency is pivotal, as it directly impacts the mechanical performance and reliability of the bilayer system. In this section, we delve into the intricate interplay between fluid loading and the consequent changes in the material properties of the paper–tape bilayer cantilever.

The B-MaC demonstrates a notable hygro-expansion when introduced to fluid environments, leading to the actuation of the cantilever. This hygro-expansion is primarily attributed to the expansion or swelling of the fibers in the filter paper as they imbibe the fluid. This process instigates the development of the internal strain within the structure. Figure 3 shows the hygro-expansive or actuation strain in the filter paper is represented as  $\epsilon_{hMAX}$  the peak strain observed at saturation. The hygro-expansive strain can be described by the following equation:

$$\epsilon_h = \epsilon_{hMAX} a^{(A)} \tag{9}$$

where  $\epsilon_{hMAX}$  is the hygro-expansive strain at saturation and A is the strain rate.

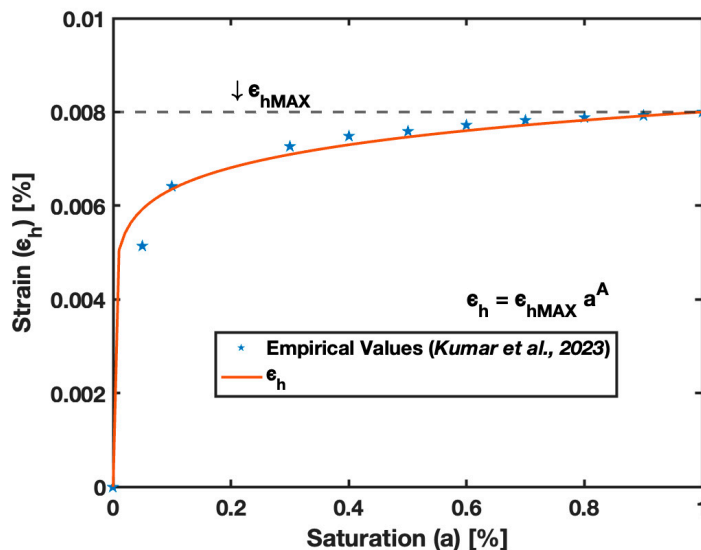


Figure 3. Hygro-expansion strain and saturation level relation for Whatman Grade 41 filter paper [24].

The material properties of B-MaC demonstrate significant variance upon wetting, particularly in the Young’s Modulus of its paper component, as uncovered in our prior research. While empirical findings highlighted the change in modulus for wetted paper, shown in Figure 4, the tape’s modulus remained unchanged. Drawing from these observations, this study presents the relation aligned with the empirically observed trends, providing a nuanced understanding of the B-MaC system’s mechanical response.

$$E_p = E_{pDRY} e^{(-Ba)} \tag{10}$$

where  $E_{pDRY}$  is the modulus of dry paper and the B is referred to as relaxation constant.

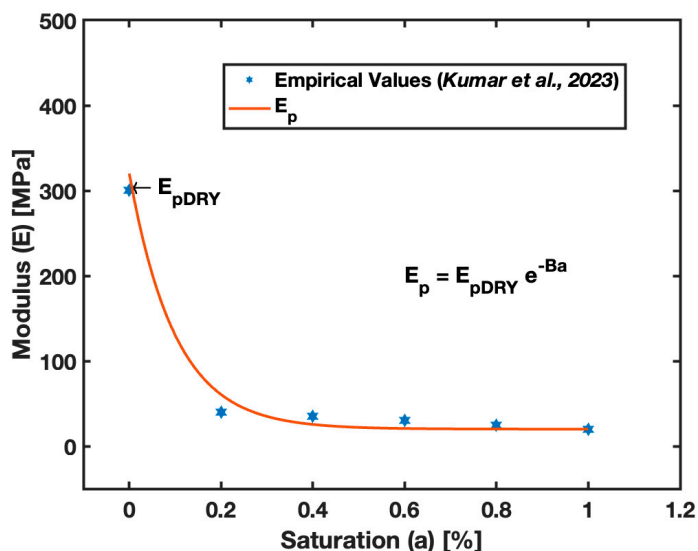


Figure 4. Modulus and saturation level relation for Whatman Grade 41 filter paper [24].

In our previous study, empirical data for the Whatman Grade 41 wetted filter paper’s modulus and hygro-expansion strain were meticulously gathered [24]. Drawing insights from these findings, these expressions align with the observed trends. These expressions of-

for a robust foundation for modeling the bilayer system’s mechanical properties, especially when one layer undergoes drastic property changes upon moisture exposure.

### 2.5. Numerical Methods

Solving the presented formulation analytically is a complex task, as it involves a non-homogeneous equation with the velocity governed by the Navier–Stokes (NS) equations based on capillary flow. To address this, we must discretize the equations for both fluid flow and bilayer actuator to obtain the coupled solution. This section will focus on the Highly Simplified Marker and Cell (HSMAC) method to determine the solution for the fluid flow within the bilayer beam. Furthermore, the velocity profile coupled with the beam equation will be used to derive the deflection via the Finite Difference Method (FDM). Subsequent subsections will elucidate the specifics of these methods and the associated boundary conditions, providing a comprehensive approach to solving the described problem.

#### 2.5.1. Velocity Analysis Using HSMAC Method

The velocity is of prime importance in this analysis, and the loading of the beam is fundamentally governed by the nature of the flow. While the analytical approach provided earlier offers a theoretical foundation, it relies on specific assumptions that may not hold true for all cases. To obtain a more accurate description of the fluid flow velocity within the domain, we will be employing the Highly Simplified Marker and Cell (HSMAC) method.

The HSMAC method can be articulated in a series of equations that adapt to our problem’s specific requirements [33]. These equations capture the detailed fluid dynamics that significantly influence the behavior of the bilayer beam. By delineating the intermediate velocity  $u^*$ , the SMAC (Simplified Marker-and-Cell) method bifurcates the Navier–Stokes Equation (6) into two distinct stages, described as follows:

$$u^* = u^n + \Delta t \left( -\frac{GP^n}{\rho} + F^n \right) \tag{11}$$

$$u^{n+1} = u^* - \Delta t \frac{G(P^n)}{\rho} \tag{12}$$

$$P^{n+1} = P^n + \delta P^{n+1} \tag{13}$$

where  $F$  and  $G$  denote the forces and gradient, respectively, and the divergence,  $D$ , of this intermediate velocity field is computed as follows:

$$Du^{n+1} = Du^* - \frac{\Delta t}{\rho} D(GP^n) \tag{14}$$

At this stage in the SMAC method, we evaluate  $D^{n+1} = 0$  and solve the Poisson equation for pressure. However, in the HSMAC method, we will utilize Newton’s method with  $D^{n+1}(P^{n+1}) = 0$  to satisfy the pressure constraint. This approach circumvents the need to solve the Poisson equation for pressure. As per Newtons method, the pressure is updated as follows:

$$P^{n+1} = P^n - \frac{D^{n+1}(u^{n+1})}{\frac{\partial D^{n+1}(u^{n+1})}{\partial P^{n+1}}} \tag{15}$$

To evaluate  $\frac{\partial D^{n+1}}{\partial P^{n+1}}$ , we substitute the value of  $Du^{n+1}$  from Equation (12) to obtain the following:

$$\frac{\partial D^{n+1}(u^{n+1})}{\partial P^{n+1}} = \frac{2\Delta t}{\rho\Delta x^2} \tag{16}$$

Combining Equations (12), (14) and (15) we obtain

$$\delta P_i^{n+1} = -\omega \frac{D^{n+1}u^{n+1}}{\frac{2\Delta t}{\rho\Delta x^2}} \tag{17}$$

where  $\omega$  is the converge acceleration coefficient and  $\delta P$  represents the correction to the pressure. However, it is crucial to emphasize that when updating the pressure, the flow rate must also be correspondingly adjusted. Both elements require simultaneous updating. The methods for flow updates using Taylor expansion and pressure updates are detailed as follows:

$$u_{i+1}^{n+1} = u_{i+1}^{n+1} + \frac{\Delta t}{\rho\Delta x} \delta P_i^{n+1} \tag{18}$$

$$u_i^{n+1} = u_i^{n+1} - \frac{\Delta t}{\rho\Delta x} \delta P_i^{n+1} \tag{19}$$

$$P_i^{n+1} = P_i^{n+1} + \delta P_i^{n+1} \tag{20}$$

The detailed analysis of the HSMAC method is provided in Appendix A; please refer to it for further information.

### 2.5.2. Response Deflection Analysis Using FDM

Having obtained flow velocity  $u^n$ , the next step is to calculate the response deflection of the beam, coupled with fluid loading. In a manner like the previous approach, the domain is discretized, and the corresponding velocity for the coordinate is used to predict the loading within a static frame by utilizing the  $n$  coordinate system. The Finite Difference Method (FDM) [22] will be employed, enabling us to rewrite the Equation (8) in a discretized form as outlined in the following equations:

Using Taylor Expansion:

Forward Difference for cells at  $i = 1$  and  $i = 2$ ,

$$\left[ \frac{w^0 - 4w^1 + 6w^2 - 4w^3 + w^4}{(\Delta x)^4} \right] + \lambda_1^2 \left[ \frac{w^0 - 2w^1 + w^2}{(\Delta x)^2} \right] = q_o \tag{21}$$

$$\left[ \frac{w^0 - 4w^1 + 6w^2 - 4w^3 + w^4}{(\Delta x)^4} \right] + \lambda_2^2 \left[ \frac{w^1 - 2w^2 + w^3}{(\Delta x)^2} \right] = q_o \tag{22}$$

Central Difference for cells  $3 \leq i \leq (n - 2)$ ,

$$\left[ \frac{w^{i-2} - 4w^{i-1} + 6w^i - 4w^{i+1} + w^{i+2}}{(\Delta x)^4} \right] + \lambda_i^2 \left[ \frac{w^{i-1} - 2w^i + w^{i+1}}{(\Delta x)^2} \right] = q_o \tag{23}$$

Backward Difference for cells at  $i = n - 1$  and  $i = n$ ,

$$\left[ \frac{w^{n-4} - 4w^{n-3} + 6w^{n-2} - 4w^{n-1} + w^n}{(\Delta x)^4} \right] + \lambda_{n-1}^2 \left[ \frac{w^{n-2} - 2w^{n-1} + w^n}{(\Delta x)^2} \right] = q_o \tag{24}$$

$$\left[ \frac{-3w^{n-4} + 76w^{n-3} - 210w^{n-2} + 204w^{n-1} - 67w^n}{101(\Delta x)^4} \right] + \lambda_n^2 \left[ \frac{-w^{n-3} + 4w^{n-2} - 5w^{n-1} + 2w^n}{(\Delta x)^2} \right] = q_o \tag{25}$$

The solution for the response deflection can be obtained from the above expression, in conjunction with the specified boundary conditions. While the expression has been simplified for ease of understanding, the solution will be derived by solving a system of  $n$  equations simultaneously using the Gauss elimination method via Row Echelon Form (REF).



$$A_2 = (\lambda_n^2 \Delta x^2 - 4) \quad (34)$$

$$A_3 = (6 - 2\lambda_n^2 \Delta x^2) \quad (35)$$

In the numerical analysis of a bilayer cantilever beam, the utilization of the imaginary grid point plays a vital role in enforcing specific boundary conditions, particularly at the fixed end where both deflection and slope must be zero. The imaginary grid point method facilitates the discretization process, allowing for the application of Finite Difference Methods such as forward difference approximation for calculating the slope. This approach not only aligns with the physical behavior of the structure but also enhances the computational stability and accuracy of the numerical solution. The method is integrated into the model for the bilayer cantilever, ensuring that the boundary conditions are met, and that the resulting numerical solution faithfully represents the coupled fluid–structure interaction problem at hand.

### 3. Results

The numerical methods employed in this study, encompassing the Highly Simplified Marker and Cell (HSMAC) method for fluid flow analysis and the Finite Difference Method (FDM) for beam deflection, serve as the cornerstone of our results. These methods were judiciously selected and adapted to tackle the intricacies of modeling a bilayer cantilever beam in the presence of fluid loading, ultimately leading to a coupled fluid–structure interaction problem. In the subsequent sections, the results are presented in a structured manner: first, the findings from the fluid flow method are detailed, shedding light on the underlying mechanics of flow within the bilayer beam; second, the response deflection analysis for the dynamic model is explored, enhancing our understanding of the loading effects within a static frame; third, we offer the comprehensive analysis of the fluidically coupled dynamic system (HSMAC coupled with FDM model) for the bilayer, with particular focus on varying properties such as modulus and hygro-expansive strain. The results derived from this numerical approach not only reaffirm the theoretical insights but also reveal several nuances specific to the characteristics of the B-MaC, providing new perspectives on the behavior of paper-based cantilevers under fluidic loading.

#### 3.1. Fluid Flow: Numerical Solution

The bilayer actuator under consideration, with a length and width of 20 mm and 4 mm, is composed of two distinct layers: paper, specifically Whatman grade 41 and Scotch tape. The bottom surface of the paper layer is laminated with the tape, creating a bi-material cantilever (B-MaC) actuator. In this system, the tape layer provides the foundation for the fluid flow to proceed without losses. For the purposes of our analysis, the fluid flow is simulated within a one-dimensional framework. The details of the interactions between the fluid and the solid structure will be discussed in further sections. These numerical results allow a detailed examination of the flow dynamics within the bilayer actuator, matching the capillary fluid flow as described by the Lucas–Washburn equation. This equation serves as the basis of the flow mechanism in our bilayer system and provides insights essential for understanding the overall behavior of the system.

Figure 6 depicts the numerical solution obtained via CFD using the HSMAC method. The plot illustrates the fluid flow profile at times 8 s, 24 s, 32 s, and 48 s. The plot depicts the pressure profiles in both dry and wet regions, capturing the wet–dry interface at the specified time. The model addresses two fluids: water and air, and the adapted Volume of Fluid (VOF) model confines the values of  $a$  to either 0 or 1. Here, 0 signifies a region that is not wet or where the fluid level has not yet been reached, while 1 indicates a wet region. Since the capillary flow model is utilized and the Lucas–Washburn (LW) equation assumes the wetted length to be 100 percent saturated, the saturation value can only be 0 or 1. The pressure profile delineates the pressure drop across the interface, a linear drop can be identified within the flow in the wet region. In contrast, the dry region exhibits

no pressure drop and remains at atmospheric pressure. Obtaining this pressure profile is crucial for verifying the suitability of our model tailored for capillary flow.

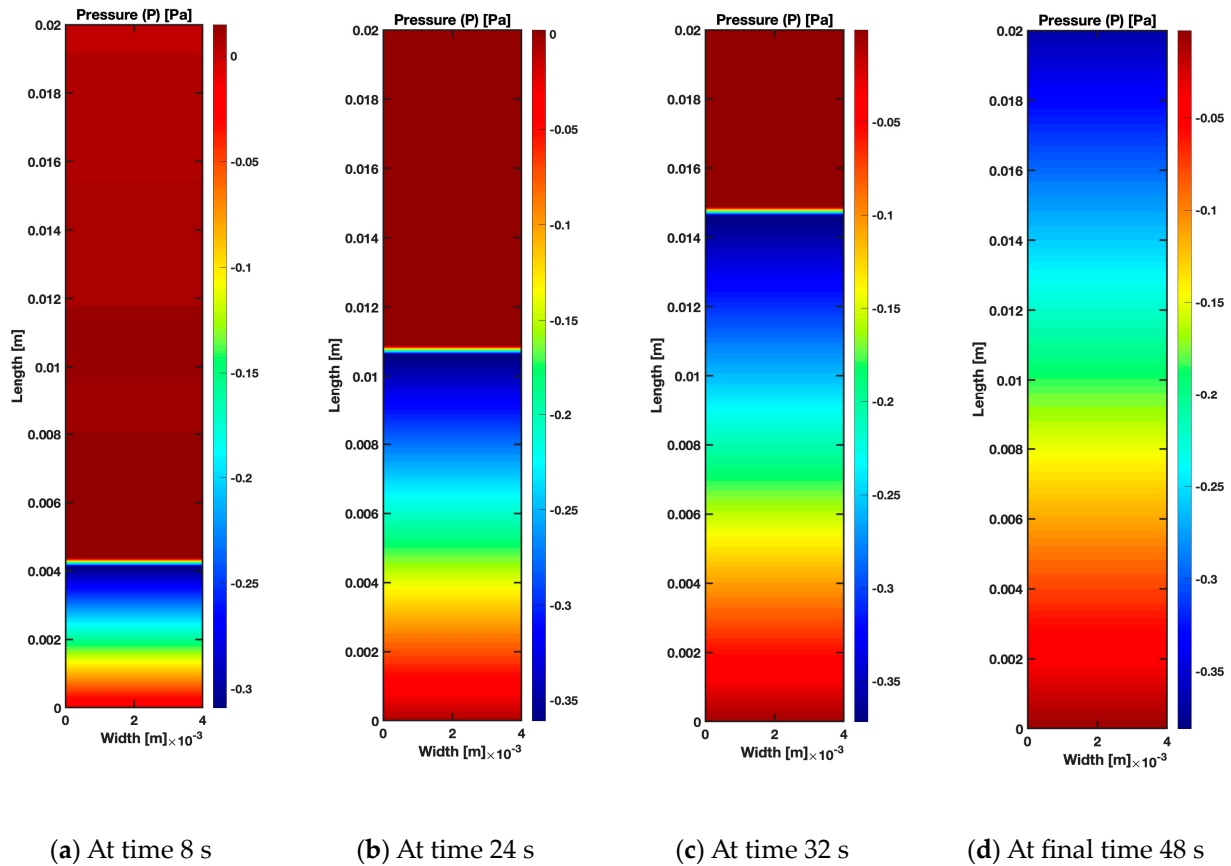


**Figure 6.** Numerical pressure profile of fluid flow in dry ( $a = 0$ ) and wet ( $a = 1$ ) regions.

The assessment is more clearly illustrated in Figure 7, showcasing a comparison between the LW (Lucas–Washburn) fluid flow model, CFD results, and empirical values documented in the previous study [24]. Figure 7 plots the wetted length  $l_w$  against time  $t$ . The empirical results, meticulously obtained, are juxtaposed with the model adopted in this study. Using the parameter  $\psi$  defined in [24] and  $\frac{C}{D}$ , the values derived for the LW model and CFD model are 8.344 and 9, respectively. These values are sufficiently close to confirm that this comparison highlights how the adapted model closely emulates the capillary action, a significant factor in the fluid flow within bilayer actuators in our investigation.

### 3.2. Dynamic Response Deflection: Numerical Solution

The dynamic response deflection analysis of the bilayer actuator assembly was conducted, and the variables are defined in Table 2. This analysis focuses specifically on the one-dimensional beam deflection to understand the response of the bilayer system. In the methodology adopted in a previous study [24], an uncoupled fluid flow as per L-W and beam dynamic deflection was presented. This uncoupled approach serves as a benchmark, aiding in the validation of the dynamically coupled fluidic response of the bilayer actuator assembly. The numerical response is obtained using the Finite Difference Method (FDM), with careful consideration given to the appropriate boundary conditions pertinent to the cantilever system. This method enables the precise calculation of the response deflection, reflecting the interactions within the system.

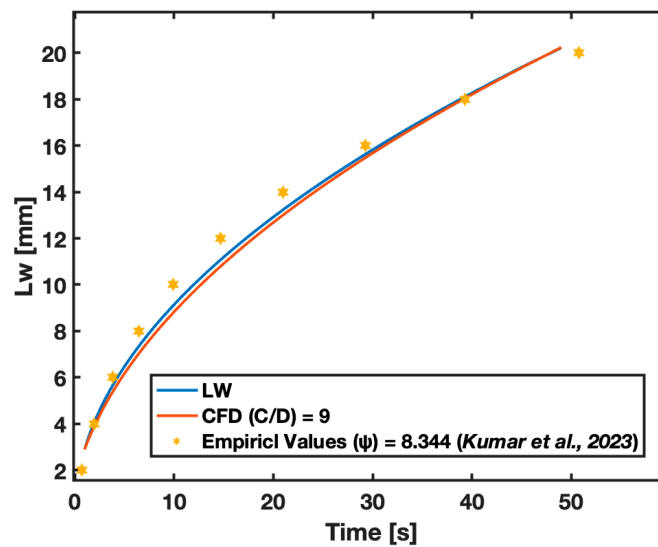


Figure 7. Comparison of LW model, CFD model, and empirical results [24].

Table 2. Variable for response deflection of B-MaC.

Variable	Value	Description/Reference
$l$	$20 \times 10^{-3}$ m	Length of bilayer actuator
$b$	$4 \times 10^{-3}$ m	Width of bilayer actuator
$h_t$	$58 \times 10^{-6}$ m	Height of tape layer
$h_p$	$220 \times 10^{-6}$ m	Height of paper layer
$E_t$	300 MPa	Modulus of tape [24]
$E_p$	20 MPa	Modulus of wet paper [24]
$\rho_f$	1000 kg/m <sup>3</sup>	Density of fluid
$\rho_t$	$1.44 \times 10^{-3}$ kg/m <sup>3</sup>	Density of tape
$\rho_p$	$85 \times 10^{-3}$ kg/m <sup>3</sup>	Density of paper
$\epsilon_o$	$2.5 \times 10^{-6}$	Effective strain of bilayer [24]

Figure 8 illustrates the dynamic response deflection of the bilayer actuator for different wetted lengths, corresponding to various time instants. The wetted lengths and corresponding deflections are obtained for the coupled fluid–structure model and the response deflection is presented for each combination of wet and dry portions of the B-MaC system.

### 3.3. Coupled Fluid Structure Model: Numerical Solution

This section focuses on the coupled fluid–structure model numerical solution. Until now, we have explored individual aspects of the system, specifically the fluid flow CFD model compared to the Lucas–Washburn (LW) equation, and the dynamic response deflection of the bilayer actuator corresponding to the wetted length. In this part of our analysis, we will present the results from a fluidically coupled flow and response deflection of the bilayer system. The fluid flow is calculated using the Highly Simplified Marker and Cell (HSMAC) method at any given time, which leads to changes in the properties of the bilayer materials. This, in turn, results in a response deflection that is iteratively obtained by employing Equation (30) for the coupled system. The following discussion elucidates the integrated approach and the insights derived from this comprehensive modeling of the bilayer actuator.

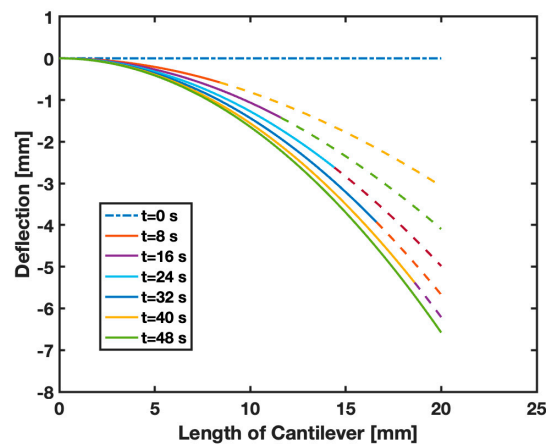


**Figure 8.** Dynamic response deflection: response deflection is plotted for different wetted lengths obtained via the Lucas–Washburn (LW) relation. The solid line represents the wetted length, while the dashed line signifies the dry length on the bi-material cantilever (B-MaC).

Figure 9a illustrates the response deflection vs. the length and width of the bilayer cantilever, showcasing the dynamic deflection of the B-MaC as the flow progresses from the fixed end to the free end of the cantilever. This 3D plot for the bilayer actuator at various wetted lengths is solved by utilizing a new coordinate approach, obtaining the velocity for each discretized cell, and iteratively solving for the dynamic response deflection of the bilayer actuator. Figure 9b presents a continuous 3D plot for the bilayer actuator under fluidic loading, representing the continuous plot and displaying the overall profile of the 1D beam over the period of loading.

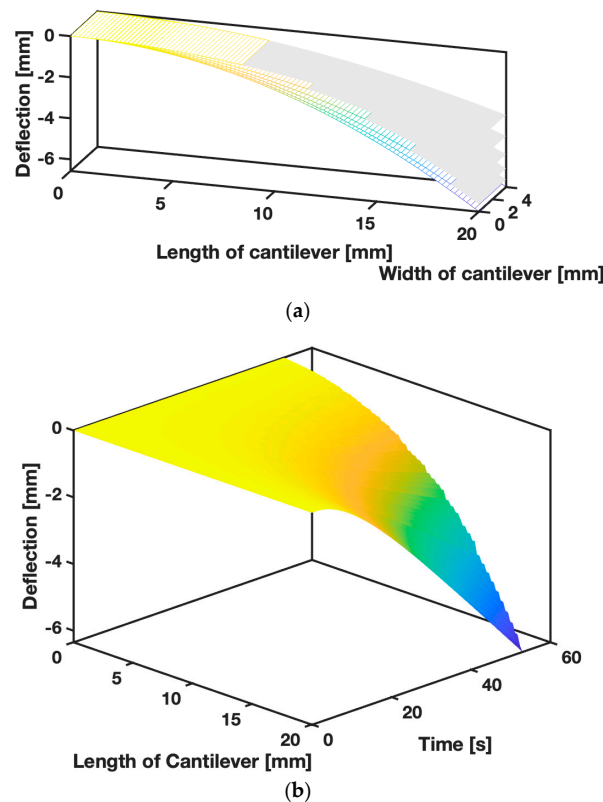


**Figure 9.** Numerical solution 3D plot of response deflection for fluidically coupled model: (a) 3D plot for bilayer actuator at various wetted lengths obtained via CFD; (b) continuous 3D plot for bilayer actuator under fluidic loading.

### 3.4. Parametric Plots

This section introduces parametric plotting to provide a nuanced visual representation of our findings. This approach enhances our comprehension of the underlying dynamics and offers a more comprehensive perspective on the behavior of the bilayer actuator assembly.

#### 3.4.1. Strain Loading Parameter ( $\zeta$ )

The strain loading resulting from the hygro-expansion of paper is treated as an internal loading mechanism within the bilayer actuator. Figure 10 displays the response deflection of the B-MaC under varying strain loading parameters, explored within a specified range.

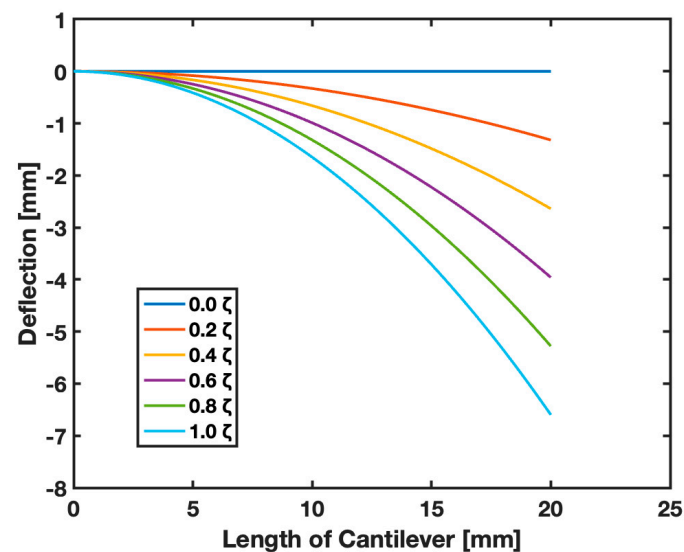


Figure 10. Response deflection of bilayer actuator for different strain loadings.

Figure 10 illustrates the variations in response deflection of the bilayer actuator due to strain loading. In this plot, strain loadings of 0, 0.2 $\zeta$ , 0.4 $\zeta$ , 0.6 $\zeta$ , 0.8 $\zeta$ , and  $\zeta$  are used, with  $\zeta$  representing the case for our study. The plot provides insight into the behavior of the bilayer actuator; as the strain loading decreases, the response deflection also diminishes due to the reduction of axial strain. This phenomenon can also be understood by considering the mismatch strain between the layers in the bilayer actuator. If the mismatch strain is less due to the use of certain materials for the bilayer actuator, the resulting deflection will be smaller. Conversely, the larger the mismatch strain, the more pronounced the deflection will be. This relationship underscores the sensitivity of the bilayer actuator's response to the specific characteristics of the materials used and offers additional avenues for fine-tuning the behavior of the device.

#### 3.4.2. Dynamic Pressure ( $\eta u^2$ )

The dynamic pressure, which symbolizes the kinetic energy per unit volume within a fluid flow, is commonly employed to articulate the forces exerted on a structure submerged in a fluid. In the context of our model, dynamic pressure terms emerge due to the fluidic loading of the system. Although these dynamic pressure terms are small in our specific model, we are scaling the terms to explore their potential effects. This exploration may be applicable to models involving higher density bilayers like tungsten or osmium as well as engineered ceramics. Figure 11 illustrates the response deflection of the B-MaC over a range of dynamic pressure values, shedding light on this intricate aspect of the system's behavior.

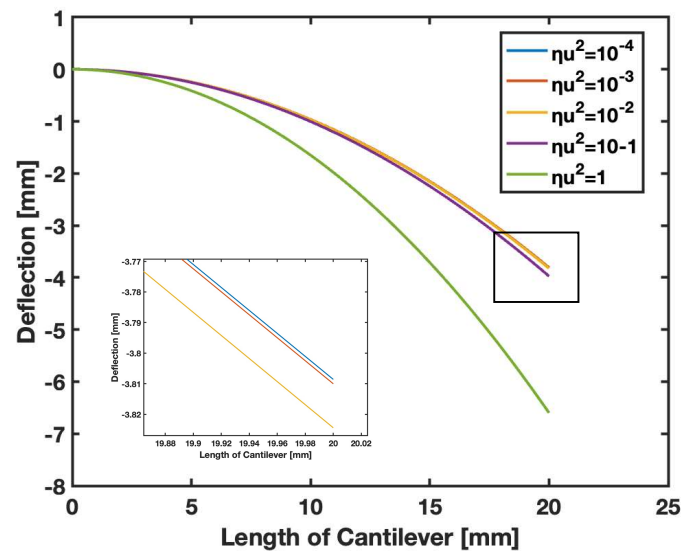


Figure 11. Response deflection of bilayer actuator for different dynamic pressure.

Figure 11 displays the influence of dynamic loading on the deflection response of the bilayer actuator. To facilitate a straightforward comparison, dynamic pressure values have been normalized. The analysis covers dynamic pressure values ranging from  $10^{-4}$  to 1, illustrating a decrease in deflection response as the dynamic pressure diminishes. The observed behavior can largely be attributed to the mass density of the bilayer cantilever, a critical factor in the system’s dynamics. The graph indicates that the actuator’s response reaches a minimal level at a converging value for dynamic pressure, beyond which further reductions have a negligible impact on the deflection response. This emerges due to the normalization of dynamic pressure, aiming to study its specific effect. As this value decreases, it results in a scenario where the impact of dynamic pressure becomes notably minor compared to the strain loading parameter  $\zeta$ . The pronounced dominance of strain loading as dynamic pressure further reduces can be corroborated by a complementary analysis presented in Figure 10.

In our study, the parameter  $\eta$  is negligible, making it significantly smaller in comparison to  $\zeta$ . As a result, the dynamic effects within the system are minimal, and the model essentially reduces to its static formulation for any given case. This illustrates the dominance of static behavior in the context of our study and provides further insight into why the dynamic effects were found to be negligible in the results. This reinforces our previous study’s findings, where we chose to adapt the quasi-static model. The minimal dynamic effects observed in the current investigation further support the validity of using a quasi-static approach in our context, aligning with the results presented in our earlier work [5,24].

### 3.5. Variable Plots

#### 3.5.1. Hygro-Expansive Strain ( $\epsilon_h$ ) as a Function of Saturation (a)

Figure 12 illustrates the response deflection of the bilayer actuator in relation to the hygro-expansion strain, as described by Equation (9). The plot presents the response deflection of the bilayer actuator for changes in hygro-expansion strain due to saturation levels of 0, 0.2, 0.4, 0.6, 0.8, and 1. As the saturation level (a) increases, the hygro-expansion strain value also increases, causing the response deflection to rise rapidly, and ultimately reach a static state. This behavior underscores the vital interplay between saturation, hygro-expansion strain, and deflection within the system.

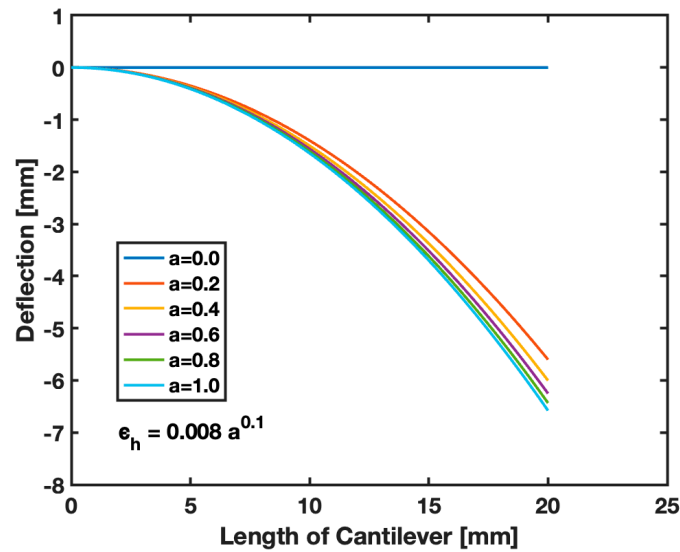


Figure 12. Bilayer actuator’s response deflection due to changes in saturation level on the hygro-expansion strain.

The change in hygro-expansion due to varying saturation levels can be effectively derived from the hygro-expansion strain and saturation level relation (Equation (9)). By utilizing this relationship, we can acquire the response deflection through the fluidically coupled model, where rapid moisture content changes in the paper due to fluid imbibition generate a corresponding deflection. This challenging task is made attainable through our model, which enables us to obtain the response deflection of the bilayer actuator at any given saturation level. Moreover, the model provides a platform to explore the effects on the actuator under various stimuli, given that these stimuli can be quantified.

3.5.2. Young’s Modulus ( $E$ ) as a Function of Saturation ( $a$ )

Figure 13 illustrates the response deflection of the bilayer actuator in relation to the modulus of the paper, as governed by Equation (10). The plot presents the response deflection of the bilayer actuator for changes in the modulus due to saturation levels of 0, 0.2, 0.4, 0.6, 0.8, and 1. As the saturation level ( $a$ ) increases, the modulus decreases, leading to a reduction in the flexural rigidity of the bilayer, and consequently causing the response deflection to increase.

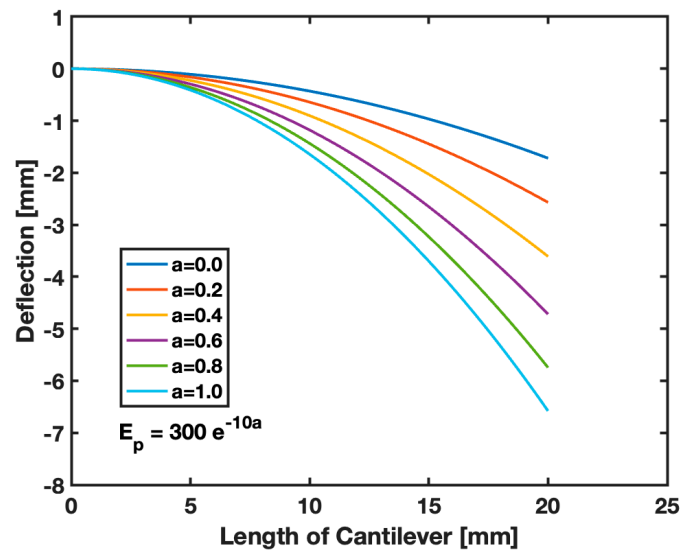


Figure 13. Bilayer actuator’s response deflection due to changes in saturation level on the modulus.

We emphasize the significant changes in the material properties of paper when wetted. Specifically, the modulus of the paper drastically reduces upon fluid imbibition. By treating the paper as isotropic and elastic under certain assumptions [5,24], we can explore the dependency of the modulus of the paper on saturation levels, further detailing how this affects the response deflection of the bilayer actuator. The plots present a greater response deflection for higher saturation content, as the modulus continues to decrease with increasing saturation level. This reduction leads to a decrease in the flexural rigidity of the bilayer actuator. A system with lower flexural rigidity is prone to deform or deflect more for a given amount of load. The results presented in Figure 13 are a clear illustration of this behavior.

### 3.6. Limiting Cases

In the study at hand, one of the primary focuses has been to build upon and validate the modeling approach through a comparison with previous research. The earlier work [2,5,24] provided a foundational understanding of the response deflection of a bilayer actuator, considering the static curvature. This static model was developed by considering the material and geometrical properties of the layers, integral to the fabrication of the actuator. The significance of the current fluidically coupled model becomes evident when observed in its limiting case.

As the bilayer actuator reaches its maximum deflection, the behavior of this dynamic system begins to resemble the static case, previously considered. To ensure the robustness of the current approach, empirical data for the static response deflection of B-MaC were also analyzed. These empirical findings served as a critical benchmark, offering tangible metrics against which the numerical predictions could be evaluated.

In Figure 14, the close agreement between the limiting case of the present fluidically coupled model, the static model, and the empirical data provided in Table 3, obtained by experiment, is prominently showcased. The similarities underscore the compatibility and coherence between different modeling approaches. Such validation does more than merely affirm the accuracy of the current model. It highlights the continuity of understanding across different studies, reinforcing the concept that the insights gleaned from static analysis continue to hold relevance even in more complex, dynamic scenarios.

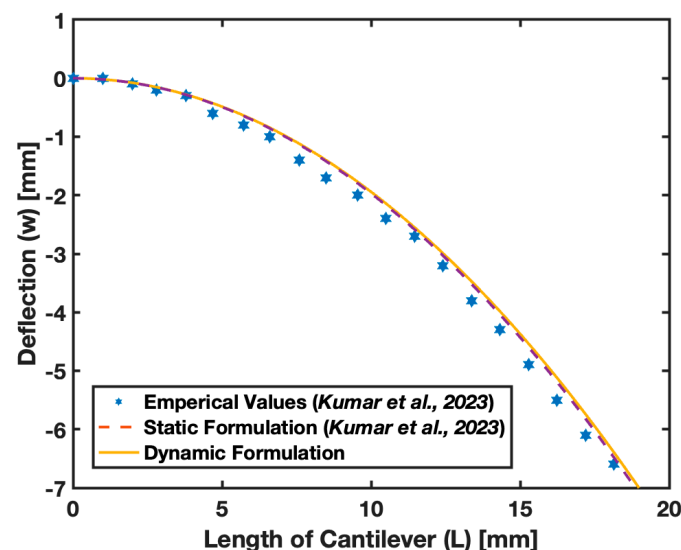


Figure 14. Comparison of fluidically coupled model with empirical and static response [24].

**Table 3.** Empirical response deflection of B-MaC [24].

Wetted length (L) mm	0.0	1.0	2.0	2.8	3.8	4.7	5.7	6.6	7.6	8.5	9.6	10.5	11.5	12.4	13.4	14.3	15.3	16.2	17.2	18.1
Response deflection (w) mm	0.0	0.0	-0.1	-0.2	-0.3	-0.6	-0.8	-1.0	-1.4	-1.7	-2.0	-2.4	-2.7	-3.2	-3.8	-4.3	-4.9	-5.5	-6.1	-6.6

This intricate comparison not only builds confidence in the current fluidically coupled model but also opens the door for further exploration and refinement. The alignment with previous studies ensures that the current research is anchored in established understanding while providing a stepping stone towards more nuanced and detailed explorations in the future.

#### 4. Discussion

The present study delved into the dynamics of bilayer actuators utilizing an advanced numerical approach, revealing intricate relationships between saturation, modulus, hygro-expansion strain, and deflection. The investigation found that response deflection sharply increases with saturation, eventually reaching a static state. This trend resonates with prior research (5, 24). Unlike traditional studies, which achieved solutions for dynamic loading without internal and external forces, our exploration confronted greater complexity due to the presence of these elements. This added complexity made closed-form solutions unfeasible. To overcome this challenge, we crafted a numerical method using the Highly Simplified Marker and Cell (HSMAC) approach for fluid flow and the Finite Difference Method (FDM) for response deflection, focusing on a fluidically coupled model of the bilayer actuator. These innovative techniques successfully aligned our findings with existing formulations for static cases and substantiated experimental data.

The fluid flow within a bilayer actuator is a complex process, inspired by our experimental observations, and modeled using Washburn's imbibition phenomenon. Comprising a hydrophilic layer (Whatman Grade 41 filter paper) and a hydrophobic layer (Scotch tape), the bilayer serves as a component of the microfluidic assay utilized for biosensing. While the paper layer is responsible for fluid imbibition, the tape layer adds rigidity to the frame, scaling the response deflection of the actuator. The results of this model, as depicted in Figure 7, reveal that the Computational Fluid Dynamics (CFD) model closely mirrors the Washburn flow. This correspondence has been experimentally validated in previous papers and proves to be suitable for our modeling. Obtaining the fluid velocity is vital as it informs the nature of the loading determined by flow conditions, an essential factor in evaluating the response of the bilayer actuator. With the velocity assessed, we advanced to solve the fluidically coupled formulation, which led to the determination of the response deflection.

The dynamic response deflection of the bilayer was solved numerically, yielding results that align with our previous research and experimental findings. Figure 8 illustrates the dynamic response deflection for various wetted lengths, and it is essential to recognize that the dynamic effects within this formulation are minimal. This leads us to conclude that the results closely mirror the static formulation as presented in previous studies. While the formulation can be considered static for most cases due to the slight dynamic effect, it is intriguing to discover outcomes that could accommodate different material types. If utilized to construct a bilayer actuator, this formulation could be applied to gauge the response deflection across a broader range of materials.

The coupled fluid–structure model for bilayer actuators accounts for changes in the modulus and hygro-expansion strain upon wetting. Since paper is hygroscopic in nature, its properties are altered due to fluid imbibition, resulting in hygro-expansion strain and a decrease in modulus. These relations, detailed in Equations (8) and (9), highlight trends at various saturation levels, aligning with the experimental values deduced in previous research. The coupled fluid model assesses the effects of different saturation levels of the paper when fluidically loaded. These properties change rapidly upon wetting, explaining why the dynamic effect is negligible in our case. This model serves as a valuable tool for assessing or quantifying a range of biosensors that operate based on external stimuli. In

our scenario, the fluid functions as the external stimulus, and by analyzing the response deflection at different saturation levels, we pave the way to quantify the response for analogous systems.

Critical loading characterizes a scenario where dynamic pressure and strain loading are equivalent. Achieving this equivalence would necessitate an exceedingly large fluid velocity, which is not a practical approach in our model given that the dynamic pressure is minimal. However, in specific practical cases where the velocity of the moving load can be defined by  $\sqrt{\frac{\zeta}{\eta}}$ , the concept of critical loading can be identified and applied. This reveals the potential complexity of the system and highlights a condition that may be relevant in different or more extreme contexts.

A comparative data analysis of the dynamic responses in B-MaC was undertaken to align our findings with the existing literature. This analysis evaluated diverse parameters, including the materials utilized, modeling techniques, key outcomes, and the extent of interaction studies, all of which are elaborated upon in Table 4. The table provides a comparative analysis of B-MaC’s dynamic responses across eight studies. Our research, utilizing Whatman Grade 41 filter paper and Scotch tape, delves into bilayer actuator dynamics through HSMAC and FDM methodologies, focusing on hygro-expansion responses. Other studies explore various facets, from tracing paper’s curling dynamics to nanowire thermal conductivity in amorphous polystyrene (a-PS). Different modeling methods are adopted, including empirical, and numerical, each study shedding light on unique interactions and bringing its own set of limitations and key findings. Across the board, there is an emphasis on understanding material dynamics under varied conditions.

**Table 4.** Comparative data analysis of dynamic responses in B-MaC.

Parameter	Our Study	Study [8]	Study [9]	Study [10]	Study [19]	Study [25]	Study [26]	Study [27]
Objective	Bilayer actuator dynamics	Curling dynamics	Bending response due to interaction with water	Swelling-induced actuation analysis	Hygro-expansive deformation analysis	Non-linear piezoelectric actuator	Microcantilever dynamic analysis	Nanowire thermal conductivity
Material used	Whatman Grade 41 filter paper and Scotch tape	Tracing paper	Filter paper	Tracing paper	Whatman Grade 1 filter paper	PZT, or lead zirconate titanate	High-density copper	Amorphous polystyrene (a-PS)
Modeling approach	HSMAC and FDM	Empirical	Numerical	Empirical	Numerical	FEA	FDM	Thermal
Interaction studied	Hygro-expansion response	Swelling response	Hygro-mechanical response	Differential swelling	Hygro-expansive swelling	Domain wall dynamics	Hydrodynamic interaction	Thermal conductance
Limitations	Small to moderate deflections only (0–10 mm)	Small deflections only	Moisture transport with constant diffusivity only	Non-swelling mediums only	Small deflections only (0–4 mm)	Phenomenological model constraints	Small deflections only (0–5 mm)	Conduction only
Key contributions	Fluid–structure interaction for bilayer actuators	Curling instability induced by swelling	Non-linear stability influence on paper	Curling of wet paper	Bending and buckling of wet paper	Electro-elastic material optimization	Fluid–coupled dynamic analysis	Thermal conductance using dual cantilevers

In this study, we primarily explored the dynamic behavior of rectangular cantilevers, a choice driven by its prevalent application and analytical convenience. However, real-world applications present a variety of cantilever shapes and sizes. While our model offers a robust foundation for rectangular configurations, its extension to other geometries, like circular or triangular, demands further scrutiny. Such expansion is critical, as different shapes introduce unique stress distributions, boundary conditions, and vibrational modes, potentially affecting the dynamic response.

## 5. Conclusions

This study elucidates the intricate dynamics of bilayer actuators using advanced numerical methods, specifically the HSMAC method and FDM, shedding light on interactions between saturation, modulus, hygro-expansion strain, and deflection.

The manuscript provides a comprehensive study on the dynamic behavior of bilayer actuators, integrating the effects of fluid flow, strain, and material properties. The fluid flow section validates the fluid flow model by comparing CFD and Lucas–Washburn (LW) outcomes against empirical results, achieving values of 9 and 8.344 respectively, underscoring the model's fidelity in simulating capillary action. The dynamic response of B-MaC elucidates the fluid–structure interaction, which is formulated through a coupled fluid–structure model. The deflection response significantly varies when subjected to strain loading. It reveals a direct relationship between axial strain and deflection, emphasizing that material selection can fine-tune actuator behavior, and the role of dynamic pressure and mass density in modulating the deflection response, identifying a minimal response threshold beyond which changes are negligible. Finally, the study results delve into the critical interplay between saturation level, hygro-expansion strain, and modulus, each influencing the deflection response of the bilayer actuator in distinct manners. The results substantiate the model's capabilities to accurately capture complex fluid–structure interactions and offer valuable insights into the sensitivities of bilayer actuator systems to various influencing factors. Moreover, the study examines dynamic response deflection in bilayer actuators and underscores the minimal dynamic effects, broadening its material applicability. The hygroscopic changes evident in the hygro-expansion strain and reduced modulus of paper augment the model's utility, especially in biosensor contexts.

In summary, this research provides a comprehensive understanding of bilayer actuators using novel methodologies and rigorous validation. The framework presented challenges conventional approaches and enhances the domain of fluid and structural dynamics. The findings serve as a foundation for future studies and highlight potential advancements in both academic research and practical applications.

**Author Contributions:** Conceptualization, A.K.; methodology, A.K.; software, A.K. and J.H.; validation, A.K. and J.H.; formal analysis, A.K. and J.H.; investigation, A.K.; resources, N.R., C.A. and M.F.; writing—original draft preparation, A.K.; writing—review and editing, A.K., N.R., C.A. and M.F.; visualization, A.K.; supervision, N.R., C.A. and M.F.; project administration, C.A. and M.F.; funding acquisition, N.R., C.A. and M.F. All authors have read and agreed to the published version of the manuscript.

**Funding:** This research received no external funding.

**Informed Consent Statement:** Not applicable.

**Data Availability Statement:** Data are contained within the article. Additional data not presented in this article are available on request from the corresponding author.

**Acknowledgments:** The authors would like to acknowledge the students, research scientists, and visiting scholars at the Microfluidics Laboratory at the University of Rhode Island for their help and support.

**Conflicts of Interest:** The authors declare no conflict of interest.

## Appendix A. Motion of Finite Beam [28]

Governing equation considering pre-stress beam:

$$-V + \left( V + \frac{\partial V}{\partial \bar{x}} d\bar{x} \right) - T\theta + \left( T + \frac{\partial T}{\partial \bar{x}} d\bar{x} \right) \left( \theta + \frac{\partial \theta}{\partial \bar{x}} d\bar{x} \right) + q d\bar{x} = \rho A d\bar{x} \frac{\partial^2 w}{\partial t^2} \quad (\text{A1})$$

The equation illustrates the forces exerted on a beam element of length  $d\bar{x}$ . Here,  $T$  represents the axial force,  $V$  is the shear force,  $q$  is the transverse force, and  $M$  stands for the moment.

Neglecting higher-order terms  $d\bar{x}^2$  appearing in conjunction with tension terms,

$$\frac{\partial V}{\partial \bar{x}} + \frac{\partial}{\partial \bar{x}}(T\theta) + q = \rho A \frac{\partial^2 w}{\partial t^2} \tag{A2}$$

In formulation, we disregard the effects of rotary inertia. Since the moment effects attributable to tension are of a higher order, the results align with those from the original beam development,  $V = \frac{\partial M}{\partial \bar{x}}$ , and using  $\theta = \frac{\partial w}{\partial \bar{x}}$ , the moment-curvature results in  $EI \frac{\partial^3 w}{\partial \bar{x}^3} = -V$ . Substituting these expressions in the equation (A2), we obtain

$$EI \frac{\partial^4 w}{\partial \bar{x}^4} - \frac{\partial}{\partial \bar{x}} \left( T \frac{\partial w}{\partial \bar{x}} \right) + \rho A \frac{\partial^2 w}{\partial t^2} = q(\bar{x}, t) \tag{A3}$$

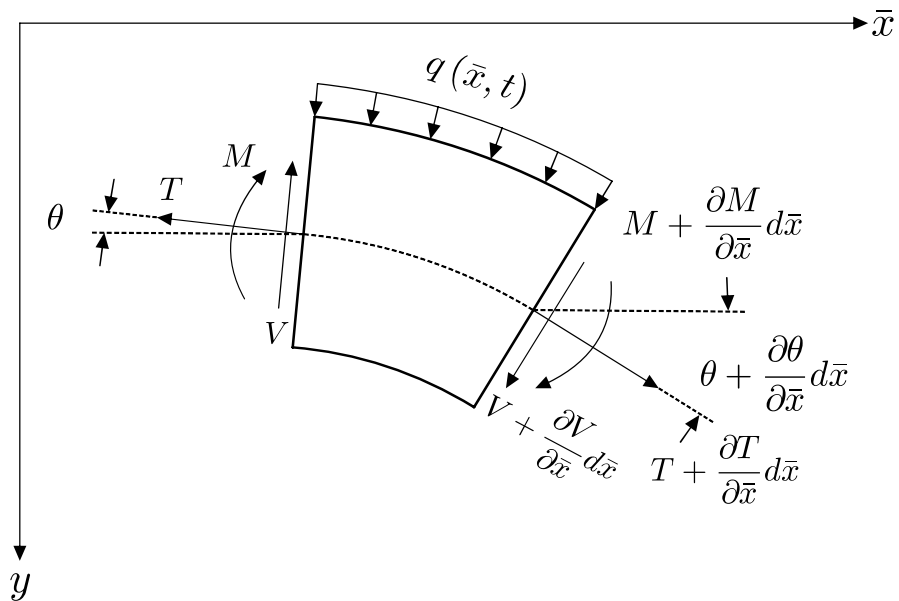


Figure A1. An element of beam under axial and transverse load.

The effects of axial strain inertia are not significant in the transverse motion. Therefore, under the assumption of constant axial tension,  $\frac{\partial T}{\partial \bar{x}} = 0$ , where  $T = EA\epsilon_0$ , the final form for the transverse equation of motion is thus

$$EI \frac{\partial^4 w}{\partial \bar{x}^4} - EA\epsilon_0 \frac{\partial^2 w}{\partial \bar{x}^2} + \rho A \frac{\partial^2 w}{\partial t^2} = q(\bar{x}, t) \tag{A4}$$

**Appendix B. HSMAC Method [33]**

Consider a 1D Navier–Stokes System of Equation:

$$\frac{\partial u}{\partial x} = 0 \tag{A5}$$

$$\frac{\partial u}{\partial t} + u \frac{\partial u}{\partial x} = -\frac{1}{\rho} \frac{\partial P}{\partial x} + \nu \frac{\partial^2 u}{\partial x^2} + F \tag{A6}$$

where  $u$  denotes the velocity of fluid flow,  $P$  represents the pressure field,  $\nu$  is the kinematic viscosity of the fluid, and  $F$  signifies the net force acting on the system.

By defining the intermediate speed, the Simple Marker and Cell (SMAC) method splits the N-S Equation into two parts:

$$\frac{u^* - u^n}{\Delta t} = -\frac{1}{\rho} \frac{\partial}{\partial x}(P^n) + \nu \frac{\partial^2}{\partial x^2}(u^n) + F^n - u^n \frac{\partial}{\partial x}(u^n) \tag{A7}$$

$$\frac{u^{n+1} - u^*}{\Delta t} = -\frac{1}{\rho} \frac{\partial}{\partial x}(P^{n+1} - P^n) \tag{A8}$$

Taking divergence on both side of Equation (A8), we obtain

$$\frac{1}{\Delta t} \left( \frac{\partial u^{n+1}}{\partial x} - \frac{\partial u^*}{\partial x} \right) = -\frac{1}{\rho} \frac{\partial^2}{\partial x^2} (P^{n+1} - P^n) \tag{A9}$$

$$\frac{\partial u^{n+1}}{\partial x} = \frac{\partial u^*}{\partial x} - \frac{\Delta t}{\rho} \frac{\partial^2}{\partial x^2} (P^{n+1} - P^n) \tag{A10}$$

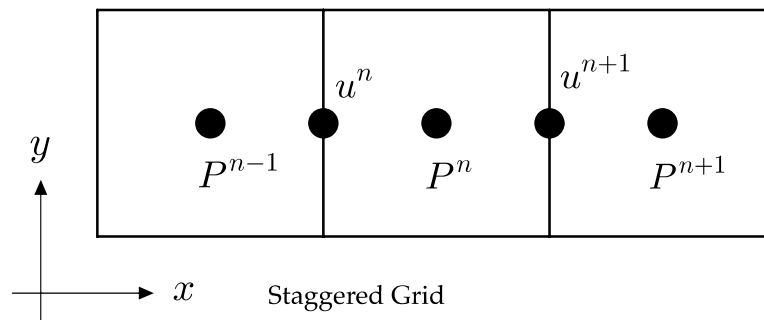


Figure A2. Staggered grid for HSMAC.

The discretization is performed solely in terms of time. By implementing spatial discretization using central difference for a staggered grid, we obtain

$$\frac{u_i^{n+1} - u_{i-1}^{n+1}}{\Delta x} = \frac{u_i^* - u_{i-1}^*}{\Delta x} - \frac{\Delta t}{\rho} \left[ \frac{P_{i+1}^{n+1} - 2P_i^{n+1} + P_{i-1}^{n+1}}{(\Delta x)^2} \right] + \frac{\Delta t}{\rho} \left[ \frac{P_{i+1}^n - 2P_i^n + P_{i-1}^n}{(\Delta x)^2} \right] \tag{A11}$$

Now writing Equation (A8) by discretizing the space, we obtain

$$\frac{u_i^{n+1}}{\Delta x} = \frac{u_i^*}{\Delta x} - \frac{\Delta t}{\rho} \left[ \frac{P_{i+1}^{n+1} - P_i^{n+1}}{\Delta x} \right] + \frac{\Delta t}{\rho} \left[ \frac{P_{i+1}^n - P_i^n}{\Delta x} \right] \tag{A12}$$

And shifting one grid,

$$\frac{u_{i-1}^{n+1}}{\Delta x} = \frac{u_{i-1}^*}{\Delta x} - \frac{\Delta t}{\rho} \left[ \frac{P_i^{n+1} - P_{i-1}^{n+1}}{\Delta x} \right] + \frac{\Delta t}{\rho} \left[ \frac{P_i^n - P_{i-1}^n}{\Delta x} \right] \tag{A13}$$

At this juncture, we diverge from the SMAC method, wherein we set  $D_i^{n+1} = \nabla u_i^{n+1}$  to zero. This leads us to proceed with solving the Poisson equations of pressure. However, in the HSMAC method, we establish  $D_i^{n+1}(P_i^{n+1})$  such that, according to Newton’s Law,  $D_i^{n+1}(P_i^{n+1}) = 0$ . By meeting the condition for  $P_i^{n+1}$ , this approach circumvents the need to solve the Poisson equation for pressure, allowing us to indirectly obtain the pressure.

As per Newtons Law,

$${}^{m+1}x = {}^m x - \frac{f({}^m x)}{f'({}^m x)} = {}^m x + \delta x \tag{A14}$$

$${}^m\delta x = -\frac{f({}^m x)}{f'({}^m x)} \quad (\text{A15})$$

Utilizing the above relation to satisfy  $D_i^{n+1}(P_i^{n+1}) = 0$ , we can obtain

$${}^{m+1}P_i^{n+1} = {}^m P_i^n - \frac{D_i^{n+1}}{\left(\frac{\partial D_i^{n+1}(P_i^{n+1})}{\partial P_i^{n+1}}\right)}_{P_i^{n+1} = {}^m P_i^n} \quad (\text{A16})$$

On evaluating  $\frac{\partial D_i^{n+1}(P_i^{n+1})}{\partial P_i^{n+1}}$ ,

$$\frac{\partial D_i^{n+1}(P_i^{n+1})}{\partial P_i^{n+1}} = \frac{\partial}{\partial P_i^{n+1}} \left( \frac{u_i^{n+1} - u_{i-1}^{n+1}}{\Delta x} \right) \quad (\text{A17})$$

$$\frac{\partial D_i^{n+1}(P_i^{n+1})}{\partial P_i^{n+1}} = \frac{1}{\Delta x} \left( \frac{\partial u_i^{n+1}}{\partial P_i^{n+1}} - \frac{\partial u_{i-1}^{n+1}}{\partial P_i^{n+1}} \right) \quad (\text{A18})$$

Substituting the value from Equations (A12) and (A13), we obtain

$$\frac{\partial D_i^{n+1}(P_i^{n+1})}{\partial P_i^{n+1}} = \frac{2\Delta t}{\rho\Delta x^2} \quad (\text{A19})$$

Combine Equations (A16) and (A19) to obtain

$${}^{m+1}P_i^{n+1} = {}^m P_i^n - \frac{D_i^{n+1}}{\frac{2\Delta t}{\rho\Delta x^2}} \quad (\text{A20})$$

$$\delta^m P_i = -\omega \frac{D_i^{n+1}}{\frac{2\Delta t}{\rho\Delta x^2}} \quad (\text{A21})$$

where is  $\omega$  the acceleration coefficient for convergence.

While updating the pressure, the flow rate must also be updated accordingly. The fluid flow  ${}^{m+1}u_i^{n+1}$  on pressure  ${}^{m+1}P_i^{n+1}$  can be obtained by Tylor expansion on the left and right side:

$$u_{i+1}^{n+1} = u_{i+1}^{n+1} + \frac{\Delta t}{\rho\Delta x} \delta P_i^{n+1} \quad (\text{A22})$$

$$u_i^{n+1} = u_i^{n+1} - \frac{\Delta t}{\rho\Delta x} \delta P_i^{n+1} \quad (\text{A23})$$

## References

1. Heidari-Bafroui, H.; Kumar, A.; Charbaji, A.; Smith, W.; Rahmani, N.; Anagnostopoulos, C.; Faghri, M. A Parametric Study on a Paper-Based Bi-Material Cantilever Valve. *Micromachines* **2022**, *13*, 1502. [[CrossRef](#)] [[PubMed](#)]
2. Gordon, C.; Kumar, A.; Heidari-Bafroui, H.; Smith, W.; Charbaji, A.; Rahmani, N.; Anagnostopoulos, C.; Faghri, M. Paper-Based Bi-Material Cantilever Actuator Bending Behavior and Modeling. *Micromachines* **2023**, *14*, 924. [[CrossRef](#)]
3. Christophersen, M.; Shapiro, B.; Smela, E. Characterization and modeling of PPy bilayer microactuators. *Sens. Actuators B Chem.* **2006**, *115*, 596–609. [[CrossRef](#)]
4. Heidari-Bafroui, H.; Kumar, A.; Hahn, C.; Scholz, N.; Charbaji, A.; Rahmani, N.; Anagnostopoulos, C.; Faghri, M. Development of a New Lab-on-Paper Microfluidics Platform Using Bi-Material Cantilever Actuators for ELISA on Paper. *Biosensors* **2023**, *13*, 310. [[CrossRef](#)]
5. Kumar, A.; Heidari-Bafroui, H.; Charbaji, A.; Rahmani, N.; Anagnostopoulos, C.; Faghri, M. Numerical and Experimental Modeling of Paper-Based Actuators. *Chem. Proc.* **2021**, *5*, 15. [[CrossRef](#)]
6. Korotcenkov, G.; Simonenko, N.P.; Simonenko, E.P.; Syssoev, V.V.; Brinzari, V. Paper-Based Humidity Sensors as Promising Flexible Devices, State of the Art, Part 2: Humidity-Sensor Performances. *Nanomaterials* **2023**, *13*, 1381. [[CrossRef](#)]
7. Yang, F.; Li, J.C.M. Diffusion-induced beam bending in hydrogen sensors. *J. Appl. Phys.* **2003**, *93*, 9304–9309. [[CrossRef](#)]

8. Douezan, S.; Wyart, M.; Brochard-Wyart, F.; Cuvelier, D. Curling instability induced by swelling. *Soft Matter* **2011**, *7*, 1506. [[CrossRef](#)]
9. Perez-Cruz, A.; Stiharu, I.; Dominguez-Gonzalez, A. Nonlinear imbibition influence on the hygro-mechanical bending response of paper due to its interaction with water. *Int. J. Non-Linear Mech.* **2017**, *97*, 89–95. [[CrossRef](#)]
10. Reyssat, E.; Mahadevan, L. How wet paper curls. *EPL (Europhys. Lett.)* **2011**, *93*, 54001. [[CrossRef](#)]
11. Wang, J.; Xu, B.; Zhu, Y.; Zhao, J. Microcantilever sensors for biochemical detection. *J. Semicond.* **2023**, *44*, 023105. [[CrossRef](#)]
12. Dkhar, D.S.; Kumari, R.; Malode, S.J.; Shetti, N.P.; Chandra, P. Integrated lab-on-a-chip devices: Fabrication methodologies, transduction system for sensing purposes. *J. Pharm. Biomed. Anal.* **2023**, *223*, 115120. [[CrossRef](#)]
13. Kara, N.; Ayoub, N.; Ilgu, H.; Fotiadis, D.; Ilgu, M. Aptamers Targeting Membrane Proteins for Sensor and Diagnostic Applications. *Molecules* **2023**, *28*, 3728. [[CrossRef](#)] [[PubMed](#)]
14. Monteduro, A.G.; Rizzato, S.; Caragnano, G.; Trapani, A.; Giannelli, G.; Maruccio, G. Organs-on-chips technologies—A guide from disease models to opportunities for drug development. *Biosens. Bioelectron.* **2023**, *231*, 115271. [[CrossRef](#)] [[PubMed](#)]
15. Kaigala, G.V.; Lovchik, R.D.; Delamarche, E. Microfluidics in the “Open Space” for Performing Localized Chemistry on Biological Interfaces. *Angew. Chem. Int. Ed.* **2012**, *51*, 11224–11240. [[CrossRef](#)] [[PubMed](#)]
16. Xu, J.; Yuan, X.G.; Li, Q.; Wang, Y.Q. Modelling and nonlinear dynamics of dielectric elastomer sandwich cantilever-plate actuators. *Eur. J. Mech. A/Solids* **2023**, *99*, 104943. [[CrossRef](#)]
17. Rasid SM, R.; Michael, A.; Pota, H.R. Dynamic modeling of a piezoelectric micro-lens actuator with experimental validation. *Sens. Actuators A Phys.* **2023**, *356*, 114344. [[CrossRef](#)]
18. Yang, X.; Kästner, P.; Käkel, E.; Smolarczyk, M.; Liu, S.; Li, Q.; Hillmer, H. Study of Dynamics in Metallic MEMS Cantilevers—Pull-In Voltage and Actuation Speed. *Appl. Sci.* **2023**, *13*, 1118. [[CrossRef](#)]
19. Lee, M.; Kim, S.; Kim, H.-Y.; Mahadevan, L. Bending and buckling of wet paper. *Phys. Fluids* **2016**, *28*, 042101. [[CrossRef](#)]
20. AAlbadawi, D.B.; Donoghue, A.J.; Robinson, D.B.; Murray, Y.M.C. Delauré, Influence of surface tension implementation in Volume of Fluid and coupled Volume of Fluid with Level Set methods for bubble growth and detachment. *Int. J. Multiph. Flow* **2013**, *53*, 11–28. [[CrossRef](#)]
21. Brackbill, J.U.; Kothe, D.B.; Zemach, C. A continuum method for modeling surface tension. *J. Comput. Phys.* **1992**, *100*, 335–354. [[CrossRef](#)]
22. Kajishima, T. *Numerical Simulation of Turbulent Flows*; Revised Edition; Yokendo: Bunkyo, Japan, 2014; Available online: <https://ci.nii.ac.jp/ncid/BB15963811> (accessed on 20 October 2023).
23. Muñoz-Galán, H.; Alemán, C.; Pérez-Madrigal, M.M. Beyond biology: Alternative uses of cantilever-based technologies. *Lab A Chip* **2023**, *23*, 1128–1150. [[CrossRef](#)]
24. Kumar, A.; Heidari-Bafroui, H.; Rahmani, N.; Anagnostopoulos, C.; Faghri, M. Modeling of Paper-Based Bi-Material Cantilever Actuator for Microfluidic Biosensors. *Biosensors* **2023**, *13*, 580. [[CrossRef](#)] [[PubMed](#)]
25. Shindo, Y.; Narita, F.; Mikami, M.; Saito, F. Nonlinear Dynamic Bending and Domain Wall Motion in Functionally Graded Piezoelectric Actuators under AC Electric Fields: Simulation and Experiment. *JSME Int. J. Ser. A* **2006**, *49*, 188–194. [[CrossRef](#)]
26. Decuzzi, P.; Granaldi, A.; Pascazio, G. Dynamic response of microcantilever-based sensors in a fluidic chamber. *J. Appl. Phys.* **2007**, *101*, 024303. [[CrossRef](#)]
27. Canetta, C.; Guo, S.; Narayanaswamy, A. Measuring thermal conductivity of polystyrene nanowires using the dual-cantilever technique. *Rev. Sci. Instrum.* **2014**, *85*, 104901. [[CrossRef](#)]
28. Graff, K.F. *Wave Motion in Elastic Solids*; Courier Corporation: Dover, UK, 1991.
29. Peng, S.; Wei, Y. On the influence of interfacial properties to the bending rigidity of layered structures. *J. Mech. Phys. Solids* **2016**, *92*, 278–296. [[CrossRef](#)]
30. Park, K.-J.; Kim, Y.-W. Vibration characteristics of fluid-conveying FGM cylindrical shells resting on Pasternak elastic foundation with an oblique edge. *Thin-Walled Struct.* **2016**, *106*, 407–419. [[CrossRef](#)]
31. Vergnaud, A.; Oger, G.; Le Touzé, D.; DeLefre, M.; Chiron, L. C-CSF: Accurate, robust and efficient surface tension and contact angle models for single-phase flows using SPH. *Comput. Methods Appl. Mech. Eng.* **2022**, *389*, 114292. [[CrossRef](#)]
32. Ha, J.; Kim, J.; Jung, Y.; Yun, G.; Kim, D.N.; Kim, H.Y. Poro-elasto-capillary wicking of cellulose sponges. *Sci Adv.* **2018**, *4*, eaao7051. [[CrossRef](#)]
33. Xiang, Y.; Yu, B.; Yuan, Q.; Sun, D. GPU Acceleration of CFD Algorithm: HSMAC and SIMPLE. *Procedia Comput. Sci.* **2017**, *108*, 1982–1989. [[CrossRef](#)]

**Disclaimer/Publisher’s Note:** The statements, opinions and data contained in all publications are solely those of the individual author(s) and contributor(s) and not of MDPI and/or the editor(s). MDPI and/or the editor(s) disclaim responsibility for any injury to people or property resulting from any ideas, methods, instructions or products referred to in the content.